Research Article

Deliang Li, Yuanjun Mai*, Wenguang Yang*, and Lidong Zhu

Late Cretaceous adakitic intrusive rocks in the Laimailang area, Gangdese batholith: Implications for the Neo-Tethyan Ocean subduction

https://doi.org/10.1515/geo-2022-0396
received March 17, 2021; accepted July 31, 2022

Abstract: The Gangdese batholith, emplaced from the Cretaceous to the Eocene in the southern Lhasa terrane of Tibet, provides critical constraints on the tectonic-magmatic evolution of the Neo-Tethyan Ocean and the India-Asia continental collision. In this article, we report new data for the Laimailang monzogranite in the southern Gangdese, including major and trace element analyses, zircon U–Pb dating, and *in situ* Hf isotope analyses. *In situ* zircon U–Pb dating of sample yielded Late Cretaceous ages (ca. 81 Ma). The monzogranite is characterized by relatively high-silica (≥56 wt% SiO_2), Na-rich, and high-Al granitoids that are characterized by high Sr, low Y and HREE contents and strongly fractionated REE patterns, with no significant Eu anomaly, indicating that they are consistent with the definition of adakite. These monzogranite have high K_2O (2.92–6.5%) and negative $\varepsilon_{Hf}(t)$ (−2.1 to −5.4), suggesting that these rocks were likely derived from the partial melting of the lower continental crust. We conclude that the Laimailang rocks of adakitic affinity were derived due to the melting of the thickened lower continental crust in the late Cretaceous.

Keywords: Late Cretaceous, adakitic rock, Neo-Tethyan, crustal thickening, Tibet

*** Corresponding author: Yuanjun Mai,** Institute of Sedimentary Geology, Chengdu University of Technology, Chengdu, 610059, China, e-mail: maiyuanjun@126.com
*** Corresponding author: Wenguang Yang,** Institute of Sedimentary Geology, Chengdu University of Technology, Chengdu, 610059, China, e-mail: yangwg1018@gmail.com
Deliang Li: College of Environment and Civil Engineering, Chengdu University of Technology, Chengdu, 610059, China; Chongqing Institute of Geological Survey, Chongqing, 401122, China
Lidong Zhu: Institute of Sedimentary Geology, Chengdu University of Technology, Chengdu, 610059, China

1 Introduction

Adakites are used to describe a group of geochemically distinct intermediate to felsic igneous rocks found generally in convergent margins; they are characterized by elevated contents of Na_2O, Al_2O_3, high-silica (≥56 wt% SiO_2), high Sr/Y (>40), and light rare earth elements (LREEs) and depletion in heavy rare earth elements (HREEs) [1,2]. Existing studies have demonstrated that rocks with adakitic geochemical properties can be produced in a variety of tectonic settings, including partial melting of subduction oceanic slab [1,3], high/low pressure differentiation of island-arc magma [4–6], and partial melting of thickened/foundered lower crust [7,8]. Therefore, the formation conditions of adakites can provide insights into nature of the convergent margins. In addition, some igneous rocks with compositions similar to adakites have been identified in continental settings [8]. Experimental studies have shown that this adakitic geochemical signature can be achieved via high-pressure melting of mafic rocks, regardless of the tectonic settings of formation [9,10].

While the India-Asia collision was thought to mainly control factor for the formation of the Tibetan Plateau, information of pre-collision geology related to the subduction of the Neo-Tethyan oceanic salb is helpful to understand structural conditions of the southern Gangdese (Figure 1). The Gangdese arc south of Lhasa is dominated by Late Triassic-Miocene mafic-felsic intrusive rocks [11–13], and the research data of the Gangdese arc intrusive rocks indicate that an early Late Cretaceous (106–80 Ma) magmatic "flare-up" event occurred in the southern Lhasa subterrane [14–16]. This event was related to subduction of the Neo-Tethyan oceanic lithosphere [15]. The geodynamic background of these related rocks continues to generate controversy, including Neo-Tethyan mid-ocean ridge subduction [15–22], Neo-Tethyan flat-slab or steep-angle subduction [14,23], and the back-arc extension of Neo-Tethyan Ocean [24]. However, the current tectonic-magmatic data are

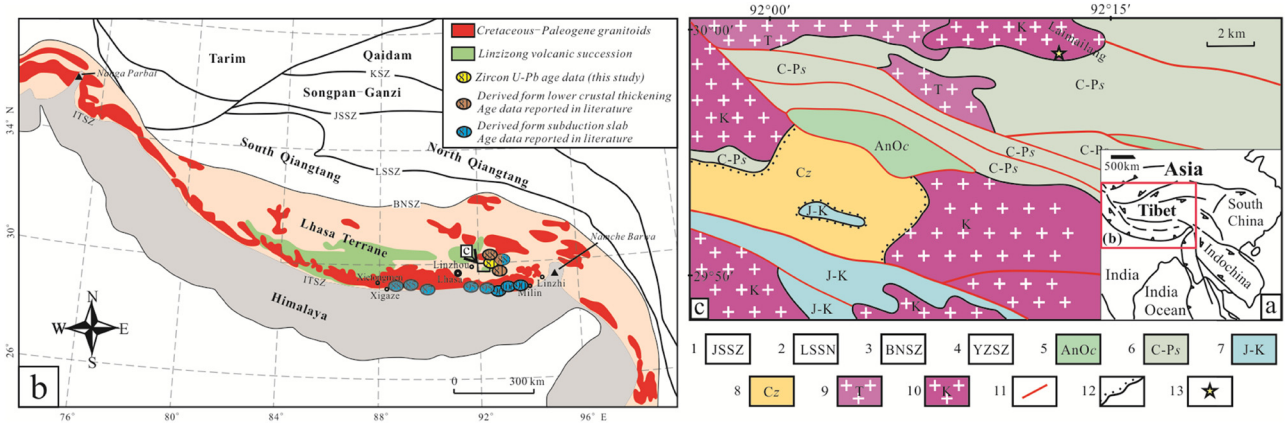

Figure 1: Simplified geological maps of (a) the position of Lhasa on the Eurasian continent, (b) the Qinghai-Tibet Plateau, and (c) the study area within the Lhasa terrane:1, Jinsha River Suture Zone; 2, Longmu Tso-Shuanghu Suture Zone; 3, Bangong-Nujiang Suture Zone; 4, Yarlung Zangbo Suture Zone; 5, Oceanic plate; 6, Carboniferous-Permian Sumdo Formation; 7, Jurassic-Cretaceous; 8, Cenozoic; 9, Triassic granitoids; 10, Cretaceous granitoids; 11, Fault; 12, Angular unconformity; and 13, Zircon U–Pb dating site in this study. Data sources: [14,15,18–20,24,46,51].

still insufficient to fully understand the tectonic evolution of the southern Gangdese during the Late Cretaceous [13–15]. The lack of consensus among those different models has also impeded our understanding of the tectonic evolution of the eastern Tethyan Ocean, especially the late-stage evolution of the Neo-Tethyan.

There is a large amount of Late Cretaceous adakites outcrop in the southern margin of the Gangdese belt, so it is an ideal place to study Late Cretaceous adakitic magmatism. Based on the different understanding of the genesis and geodynamic background of the Late Cretaceous adakite, in this study, we rationalized the contradictions by synthesizing previous studies and used field petrological observations in combination with zircon U–Pb dating and geochemical characterization of the Laimailang granitoids to discuss the genesis of the Gangdese adakitic magma and the evolution process of the Neo-Tethyan Ocean in the Late Cretaceous.

2 Geological background and samples

Geologically, the Tibetan Plateau is essentially composed of four continental blocks or terranes from south to north: the Tethyan Himalaya, Lhasa, Qiangtang, and Songpan-Ganze, separated by the Yarlung-Tsangbo suture zone, Bangong-Nujiang suture zone, and Jinsha River suture zone, respectively [25]. Prior to the Carboniferous-Permian, the Lhasa terrane was located on the northern edge of Gondwana and correlated paleo-geographically with Australia [26]. Ahead of the India-Asia collision, the Lhasa terrane underwent an Andean-type orogeny, during which the Neo-Tethyan oceanic slab subducted northward beneath the Eurasian plate in the Late Triassic through Early Paleogene [20,27]. This was comprised predominantly of Paleozoic-Paleogene sedimentary strata associated with igneous rocks [28], including a series of Mesozoic–Cenozoic magmatic rocks widespread along its southern margin that form the well-known Gangdese batholith, distributed in an east-west orientation that is nearly parallel to the Yarlung-Tsangbo River suture zone from Xietongmen to Milin. Previous studies indicated that the Gangdese batholith consist of a wide range of compositions from gabbro to granite [29] and have geochemically comparable to the calc-alkaline granitoids that were emplaced in circum-Pacific regions [30,31]. Meanwhile, the Gangdese batholith recorded a long, punctuated history of magmatism spanning ~210–40 Ma, with peak episodes of granitoid plutonism at 106–80 Ma and the subsequent period of magmatic quiescence (80–65 Ma) events, while the Linzizong volcanic successions were mainly erupted at 65–42 Ma [11,13,14,16,17,20,29]. The southern Lhasa subterrane also contains sedimentary deposits and volcanic rocks, including Cenozoic ultrapotassic volcanic rocks, the Lower Jurassic Yeba Formation, and Upper Jurassic-Lower Cretaceous Sangri Group [13,29].

The study area, located in the Gangdese batholith on the southern margin of the Lhasa terrane (Figure 1a and b), has well-preserved Mesozoic magma that records the evolution process of the Neo-Tethyan ocean. These are primarily Triassic and Cretaceous magmatic rocks, along with some Jurassic-Cretaceous strata including a series of basic to acidic volcanic rocks with island-arc geochemical characteristics. The basement is poorly exposed and includes late Paleozoic and Mesozoic units, Fragments of

ophiolites and sedimentary basement from the Carboniferous-Permian Sumdo Formation are also distributed within the study area, consisting of metamorphosed quartz sandstone and muscovite-quartz schist (Figure 1c). The Mesozoic units represent a series of basic-to-acidic volcanic rocks with island-arc geochemical characteristics.

3 Analytical methods

3.1 *In situ* zircon U–Pb LA-inductively coupled plasma mass spectrometry (ICP-MS) analyses

Zircons were separated from sample D2053-18-N1 by standard density and magnetic separation and then fixed with a standard zircon with epoxy resin. The surface of the sample target was polished until approaching the near-center section of the zircon crystal, and then a cathodoluminescence (CL) photograph was taken. *In situ* zircon U–Pb dating was conducted using an LA-ICP-MS at the Beijing GeoAnalysis using the analytical conditions defined by Yuan et al. [32]. Offline processing was performed using ICPMS Data Cal 11.5 software [33], and normal lead correction was performed on the test data [34]. Harmonic plot mapping and weighted mean age calculation were performed using Isoplot 3.0 [35].

3.2 Major and trace elements

These were trimmed to remove weathered surfaces, cleaned with deionized water, crushed, and powdered in an agate mill. The samples for geochemical analysis were ground to

Figure 2: Representative petrographical images of the Laimailang monzogranite (a, b) field occurrences; (c–f) representative microstructures of granitoid: Qtz, quartz; Am, amphibole; Bt, biotite; Pl, plagioclase; Kfs, potassium feldspar.

pass through a 200-mesh sieve and then further ground and homogenized in an agate mortar under alcohol. Major elements were analyzed by X-ray fluorescence (XRF), and trace and rare earth elements were analyzed by ICP-MS at the ALS Mineral-ALS Chemex Laboratory (Guangzhou, China). Major elements were assayed using a RIX-2100 XRF spectrometer, with an analytical precision of ±5%. Trace element concentrations (rare earth elements included) were assayed using an Agilent 7500a ICP-MS. The precision of the ICP-MS analyses is ±10% for all elements, but some are ±5%.

3.3 *In situ* zircon Hf isotope analysis

In situ Hf isotope measurements were taken on zircon grains at the same position as previously dated, using a Thermo Scientific Neptune (Plus) multi-collector-ICP-MS, coupled with a New Wave 193 nm solid-state laser ablation system at Beijing GeoAnalysis (Beijing, China). After removing ages with anomalies (≤95% confidence level), Hf isotopic compositions were determined for the remaining samples. Lu-Hf isotopic measurements on zircon were performed by LA-MC-ICP-MS with a beam size of 38 μm, an energy density of 10–11 J/cm^2, and a laser pulse frequency of 10 Hz.

4 Results

4.1 Petrography

We focused on the Laimailang intrusive rocks that contain a number of regional structural features and ductile shear zones that are oriented approximately E–W (Figure 1c). Weathered surfaces are khaki in color, whereas fresh surfaces are gray and show a massive structure, and five samples were collected from rocks without visible alteration (Figure 2). They had a hypidiomorphic granular structure, with a mineral composition of mostly plagioclase (40%), potassium feldspar (25%), quartz (25%), amphibole (5%), and biotite (<5%), with apatite and zircon as an accessory mineral (Figure 2). Plagioclase is semi-idiomorphic plate, most of those have zoned crystal structure, and a small amount of the crystals have weak clay alteration (Figure 2c). Potassium feldspar is microcline in the shape of other granular, and part of the crystal contains plagioclase, hornblende, and biotite, which constitute the intergrowth textures (Figure 2d–f). Quartz crystals are similar in size to feldspar and fill between feldspar crystals (Figure 2e and f). Amphibole and biotite are rare, and chlorite alteration was found in some edges (Figure 2c). The granitic structure of the sample is complete and identified as monzogranite in QAP classification diagram (Figure 3a).

4.2 Whole-rock geochemistry

The original whole-rock major and trace element data are shown in Table 1 as standardized values. The loss on ignition (LOI) values of the five samples were all <1%, indicating only weak effects from weathering and erosion. The studied samples have acidic composition, showing SiO_2 ranging ~65–68 wt%, in association with high Na_2O (3.41–4.07 wt%), Al_2O_3 (14.95–16.60 wt%), and K_2O (mostly

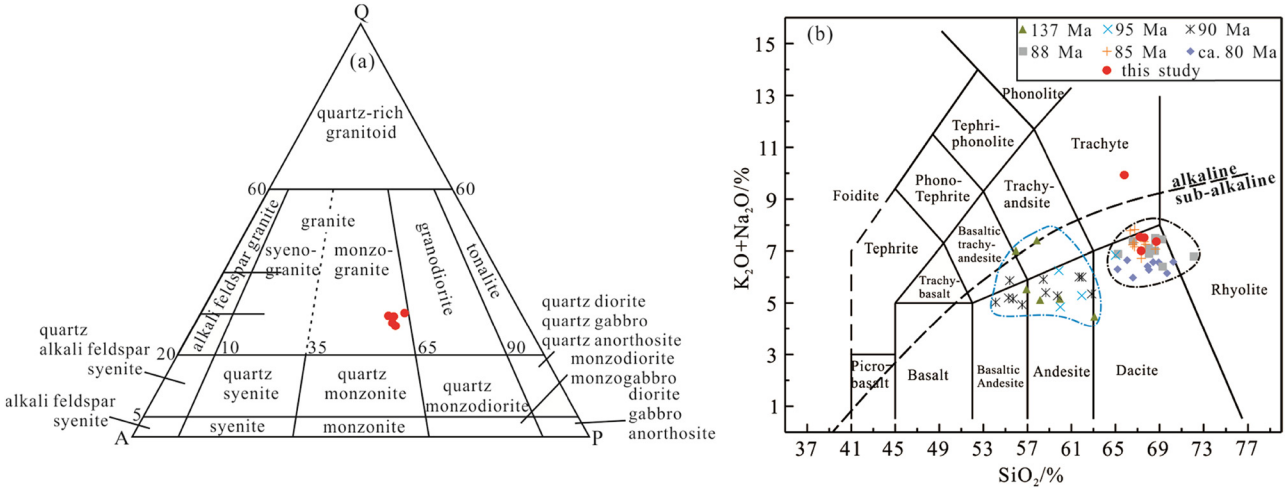

Figure 3: (a) QAP classification and (b) TAS diagram [40] for the Laimailang monzogranite.

Table 1: Bulk-rock geochemical compositions of Laimailang monzogranite (major elements: wt%; trace elements: ppm)

Sample	D2053-18-DH1	D2053-18-DH2	D2053-18-DH3	D2053-18-DH4	D2053-18-DH5
SiO_2	64.57	67.29	66.65	66.61	68.33
TiO_2	0.43	0.52	0.56	0.54	0.48
Al_2O_3	16.32	15.45	15.49	15.35	14.9
TFe_2O_3	3.15	3.79	3.81	3.94	3.55
MnO	0.06	0.07	0.07	0.08	0.07
MgO	1.36	1.71	1.77	1.82	1.61
CaO	2.48	3.15	3.61	3.22	3.16
Na_2O	3.35	3.71	4.04	3.72	3.65
K_2O	6.39	3.77	2.9	3.75	3.67
P_2O_5	0.2	0.24	0.26	0.25	0.22
LOI	0.56	0.51	0.45	0.5	0.64
Total	98.87	100.21	99.61	99.78	100.28
Sc	5	6	6	6	6
V	57	68	72	69	64
Cr	26	30	30	30	28
Co	7	9	9	10	8
Ni	10	10	12	12	10
Rb	176.5	145	118.5	143.5	136
Ba	2,510	735	436	802	471
Th	12.1	20.6	19.95	21.2	15.1
U	1.7	2.39	2.15	2.26	2.43
Nb	10.5	10.9	12	11.4	10.8
Ta	0.9	0.9	0.9	0.9	0.9
La	31.8	43.3	54	46.5	37.3
Ce	67.5	78.9	91.7	82	70.9
Pb	25	19	17	20	18
Pr	7.71	8.12	9.3	8.5	7.69
Sr	985	819	815	823	739
Nd	28.4	29.1	32.9	30	27.7
Zr	146	156	199	163	152
Hf	3.8	4	5.5	4.3	4
Sm	4.69	4.75	5.2	4.83	4.52
Eu	1.27	1.19	1.33	1.26	1.13
Ti	2,577	3,117	3,357	3,237	2,877
Gd	3.34	3.35	3.61	3.37	3.18
Tb	0.44	0.42	0.47	0.42	0.39
Dy	2.1	2.04	2.21	2.15	2.03
Y	11	10.8	11.7	11	10.6
Ho	0.38	0.37	0.41	0.4	0.38
Er	1.14	1.07	1.15	1.12	1.05
Tm	0.16	0.15	0.18	0.16	0.15
Yb	0.98	0.94	1.06	0.98	0.9
Lu	0.14	0.14	0.17	0.15	0.14
Mg#	46.1	47.2	47.9	47.8	47.3
Sr/Y	89.55	75.83	69.66	74.82	69.72
$(La/Yb)_N$	148.98	165.96	187.74	166.33	168.89

$Mg^{\#}$ = Mg/(FeO + MgO); LOI = loss on ignition *N* is chondrite-normalized [60].

2.92–3.78 wt%, except D2053-DH1 6.50 wt%), low MgO (1.38–1.83 wt%), and medium $Mg^{\#}$(46–48). On the total alkalis versus silica (TAS) diagram [40], samples mostly plot in the dacite fields, with only sample D2053-DH1 plotting in the trachyte field (Figure 3b). The samples are dominantly high-K calc-alkaline (Figure 4a), and they have metaluminous affinity on the plot of A/CNK versus A/NK (Figure 4b).

All samples presented marked fractionated REE patterns in chondrite-normalized REE diagrams and primitive mantle-normalized trace element spider diagrams (Figure 5). They had low HREEs and Y but relatively high (La/Yb)N, being enriched in LREEs and depleted in HREEs (Table 1), which have strong similarity with the typical adakite (Figure 5a). Samples relatively enriched in large ion lithophile elements (LILEs: Rb, Th, K, Pb, Sr, etc.) and depleted in high-field strength elements (HFSEs: Nb, Ta, Ti, etc.) (Figure 5b).

4.3 Zircon U–Pb ages and Hf isotopes

LA-ICP-MS U–Pb data from zircon were determined in 35 groups of ages (Table 2). The zircon grains are mostly euhedral, with elongated habits (crystal lengths of 60–120 μm) and length-to-width ratios from 2:1 to 3:1. Most zircons are generally transparent and colorless. The CL images show oscillatory and planar magmatic growth zoning with broadly homogeneous cores (Figure 6a), which are very similar to the zircon morphology of typical granitoids [36]. Their Th and U concentrations ranged from 327 to 965 and 519 to 930 ppm, respectively, yielding Th/U ratios of 0.63–1.08 that indicated igneous zircons [37]. Weighted means of pooled $^{206}Pb/^{238}U$ ages were taken to represent the crystallization ages reported with 95% confidence level. Of these, eight zircons had a harmonicity of <95% and were not used further in the harmonic age calculation. The $^{206}Pb/^{238}U$ weighted age of the remaining 27 zircons was 81.22 ± 0.49 Ma (n = 27, MSWD = 0.4) (Figure 6b), placing the crystallization ages of the monzogranite in the Late Cretaceous.

A total of 27 *in situ* Hf isotope analyses were successfully undertaken on zircons within sample D2053-18-N1 (Table 3), and initial $^{176}Hf/^{177}Hf$ ratios were calculated on the basis of the $^{206}Pb/^{238}U$-weighted age (81 Ma). The $^{176}Hf/^{177}Hf$ ratio obtained for zircon standard GJ-1 during the data acquisition was 0.282005 ± 34 (2 standard deviations, n = 6), in good agreement with the recommended Hf isotopic ratio [38]. The decay constant used for ^{176}Lu was 1.867×10^{-11} [39]. These zircons were characterized by distinctly negative initial $\varepsilon_{Hf}(t)$ values (−2.1 to −5.4) and yielded $^{176}Hf/^{177}Hf$ ratios of 0.282661–0.282568. Zircon D2053-18-N1-14 had the lowest initial $\varepsilon_{Hf}(t)$ value.

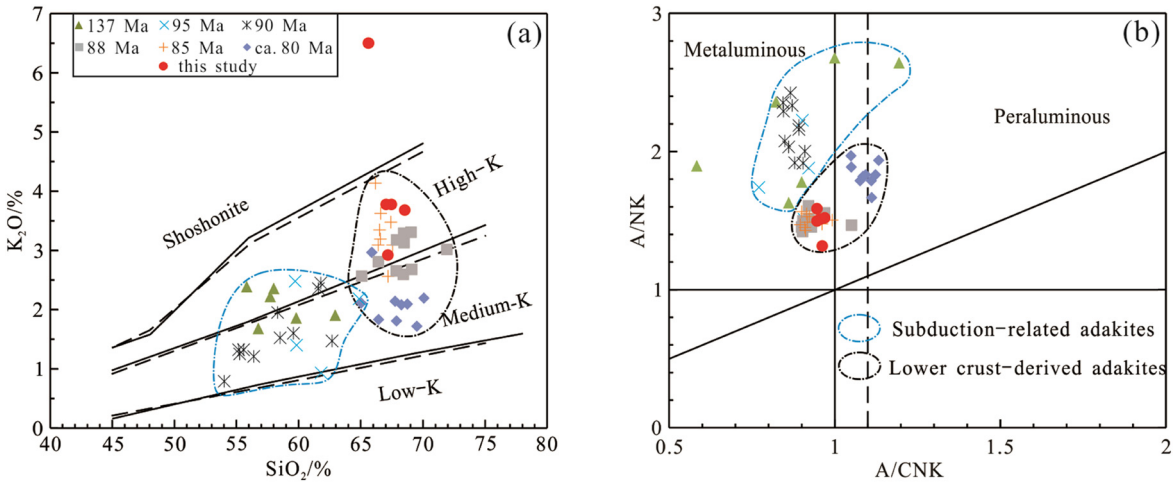

Figure 4: Laimailang monzogranite sample classification within (a) K_2O vs SiO_2 diagram and (b) A/NK vs A/CNK diagram, with other results for comparison.

5 Discussion

5.1 Petrogenesis and tectonic setting

The data presented herein show that the studied Laimailang intrusive suite consists of high-silica (≥56 wt% SiO_2), Na-rich, and high-Al granitoids that are characterized by high Sr, low Y, and HREE contents, and strongly fractionated REE patterns, with no significant Eu anomaly (Figure 5a), indicating that they are consistent with the definition of adakite [2]. In addition, all samples for the studied rocks plot within the adakite area on the Sr/Y vs Y diagram (Figure 7a) and $(La/Yb)_N$ vs Yb_N diagram (Figure 7b), indicating the adakitic feature.

As shown in Figure 5, all samples of Laimailang pluton rocks exhibit similar characteristics, indicating that all samples could have been derived from a common magma source region. Several lines of evidence indicate that the Laimailang monzogranite are most likely derived from partial melting of thickened lower crust.

(1) The fractional crystallization of amphibole can significantly increase the ratio of Sr/Y to La/Yb and reduce the content of HREEs and Y [4]. However, it has less influence on the partition coefficient of HREEs than middle rare earth elements (MREEs) [10], generating concave downwards patterns between MREEs and HREEs [4,5]. The Laimailang pluton did not show this "U-shaped" partition curve (Figure 5a). Trace element signatures for the Laimailang monzogranite are consistent with the formation of lower crust rather than subducted slab (Figure 8). Our samples showed that the remarkable HREE depletion in the Laimailang monzogranite, as attested by the elevated Sr/Y, $(La/Yb)_N$, and $(Gd/Yb)_N$ (>1) values, is indicative of

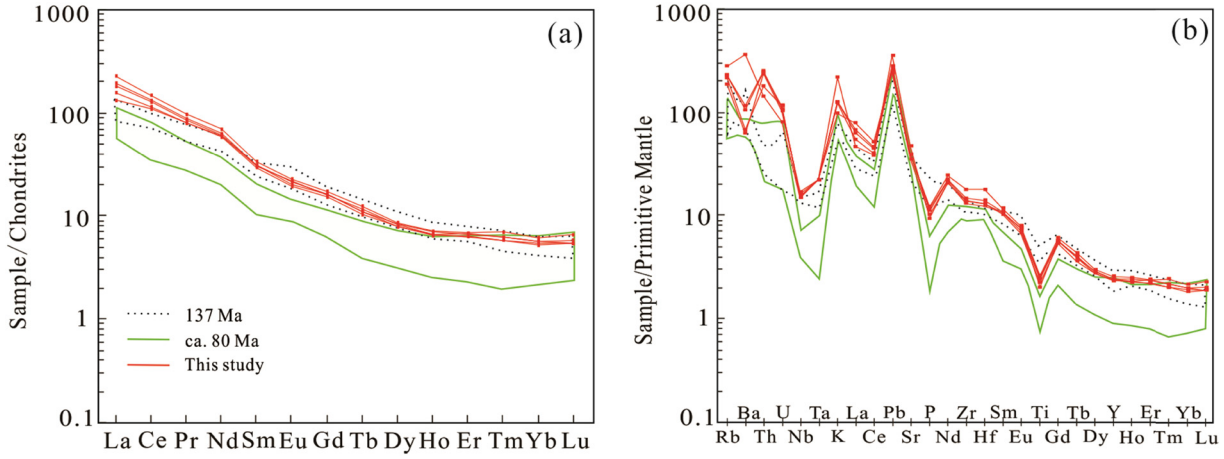

Figure 5: Laimailang monzogranite (a) chondrite-normalized REE patterns and (b) primitive mantle-normalized trace element spider diagrams (normalization values after [59]).

Table 2: LA-ICP-MS zircon U–Pb analytical results from Laimailang monzogranite

Spot	Pb	Th	U	Th/U	Age (Ma)										Confidence level (%)
		($\times10^{-6}$)			$^{207}Pb/^{206}Pb$	±1σ	$^{207}Pb/^{235}U$	±1σ	$^{206}Pb/^{238}U$	±1σ	$^{207}Pb/^{235}U$	±1σ	$^{206}Pb/^{238}U$	±1σ	
D2053-18 monzogranite															
1	12.16	681	698	0.98	0.0520	0.0041	0.0914	0.0066	0.0129	0.0002	89	6	83	1	92
2	12.97	729	736	0.99	0.0534	0.0024	0.0935	0.0047	0.0127	0.0002	91	4	81	1	89
3	11.40	516	677	0.76	0.0520	0.0028	0.0903	0.0049	0.0128	0.0003	88	5	82	2	92
4	13.16	645	762	0.85	0.0493	0.0019	0.0885	0.0038	0.0130	0.0002	86	4	83	2	96
5	16.69	965	930	1.04	0.0488	0.0017	0.0859	0.0032	0.0128	0.0002	84	3	82	1	98
6	8.32	367	499	0.74	0.0502	0.0019	0.0870	0.0031	0.0127	0.0002	85	3	81	1	96
7	11.91	602	677	0.89	0.0480	0.0020	0.0846	0.0041	0.0127	0.0002	82	4	81	1	98
8	15.57	918	849	1.08	0.0474	0.0017	0.0826	0.0029	0.0127	0.0002	81	3	81	1	99
9	9.22	398	531	0.75	0.0548	0.0028	0.0963	0.0050	0.0128	0.0003	93	5	82	2	87
10	12.03	612	669	0.91	0.0501	0.0024	0.0877	0.0047	0.0127	0.0002	85	4	82	1	95
11	11.66	521	675	0.77	0.0474	0.0021	0.0841	0.0040	0.0129	0.0002	82	4	82	2	99
12	10.35	457	594	0.77	0.0497	0.0028	0.0861	0.0041	0.0127	0.0002	84	4	82	1	97
13	9.59	434	568	0.76	0.0543	0.0025	0.0948	0.0045	0.0127	0.0002	92	4	81	1	87
14	11.11	495	659	0.75	0.0495	0.0021	0.0859	0.0035	0.0127	0.0002	84	3	81	1	96
15	8.71	355	524	0.68	0.0495	0.0024	0.0863	0.0042	0.0127	0.0002	84	4	82	1	97
16	15.35	845	882	0.96	0.0484	0.0014	0.0840	0.0028	0.0125	0.0002	82	3	80	1	98
17	13.71	681	807	0.84	0.0483	0.0020	0.0830	0.0032	0.0125	0.0002	81	3	80	1	99
18	9.27	407	570	0.71	0.0460	0.0017	0.0802	0.0030	0.0127	0.0002	78	3	81	1	96
19	14.00	798	812	0.98	0.0495	0.0015	0.0852	0.0029	0.0125	0.0002	83	3	80	1	96
20	8.05	345	486	0.71	0.0537	0.0031	0.0938	0.0055	0.0127	0.0002	91	5	81	1	88
21	9.43	445	571	0.78	0.0478	0.0023	0.0829	0.0038	0.0127	0.0002	81	4	82	2	99
22	15.17	864	858	1.01	0.0472	0.0015	0.0831	0.0029	0.0128	0.0002	81	3	82	1	99
23	12.01	594	723	0.82	0.0479	0.0020	0.0831	0.0037	0.0126	0.0002	81	3	81	1	99
24	9.50	536	564	0.95	0.0482	0.0022	0.0859	0.0043	0.0129	0.0003	84	4	83	2	98
25	9.93	466	600	0.78	0.0493	0.0021	0.0873	0.0036	0.0129	0.0002	85	3	83	1	97
26	14.88	790	884	0.89	0.0470	0.0017	0.0819	0.0034	0.0127	0.0002	80	3	81	1	98
27	10.73	450	672	0.67	0.0484	0.0020	0.0845	0.0038	0.0127	0.0002	82	4	81	1	98
28	7.64	333	485	0.69	0.0453	0.0026	0.0777	0.0043	0.0127	0.0002	76	4	81	2	93
29	11.47	587	700	0.84	0.0479	0.0020	0.0826	0.0037	0.0126	0.0002	81	3	81	1	99
30	9.05	452	548	0.82	0.0534	0.0023	0.0926	0.0043	0.0125	0.0002	90	4	80	1	88
31	12.67	586	793	0.74	0.0482	0.0020	0.0838	0.0038	0.0126	0.0002	82	4	81	1	98
32	10.95	670	618	1.08	0.0477	0.0022	0.0840	0.0041	0.0128	0.0002	82	4	82	1	99
33	8.11	327	519	0.63	0.0472	0.0018	0.0811	0.0034	0.0125	0.0002	79	3	80	2	98
34	11.28	507	696	0.73	0.0464	0.0016	0.0804	0.0032	0.0126	0.0002	78	3	81	1	97
35	8.22	344	513	0.67	0.0499	0.0022	0.0863	0.0041	0.0125	0.0002	84	4	80	1	95

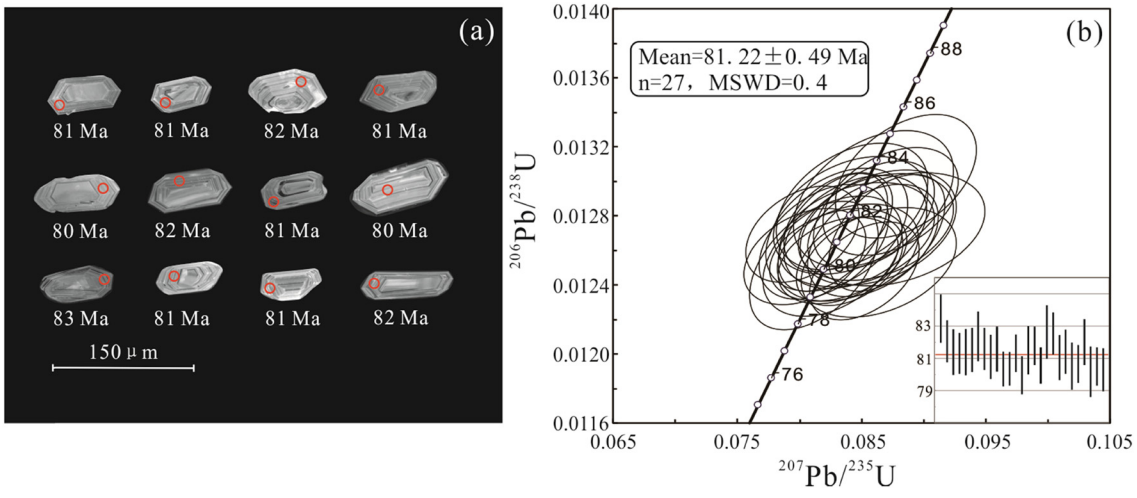

Figure 6: (a) CL images and (b) U–Pb concordia diagrams for zircon from the Laimailang monzogranite.

Table 3: Zircon Hf isotopic compositions of the Laimailang monzogranite (D2053-18-N1)

No	$^{176}Yb/^{177}Hf$	$^{176}Lu/^{177}Hf$	$^{176}Hf/^{177}Hf$	2σ	$^{176}Hf/^{177}Hf_t$	$\varepsilon_{Hf}(0)$	$\varepsilon_{Hf}(t)$	T_{DM}	T_{DM}^{C}	$f_{Lu/Hf}$
D2053-18-N1										
D2053-18-N1-04	0.016388	0.000114	0.000758	0.000018	0.282597	−6.2	−4.4	920	1,426	−0.98
D2053-18-N1-05	0.015949	0.000232	0.000720	0.000017	0.282655	−4.1	−2.3	837	1,295	−0.98
D2053-18-N1-06	0.019077	0.000307	0.000858	0.000016	0.282600	−6.0	−4.3	917	1,418	−0.97
D2053-18-N1-07	0.014031	0.000222	0.000628	0.000017	0.282620	−5.4	−3.6	885	1,375	−0.98
D2053-18-N1-08	0.018160	0.000354	0.000798	0.000017	0.282643	−4.5	−2.8	856	1,323	−0.98
D2053-18-N1-10	0.021404	0.000101	0.000952	0.000016	0.282630	−5.0	−3.3	878	1,353	−0.97
D2053-18-N1-11	0.021111	0.000486	0.000991	0.000016	0.282632	−4.9	−3.2	876	1,348	−0.97
D2053-18-N1-12	0.016582	0.000139	0.000790	0.000016	0.282592	−6.3	−4.6	927	1,436	−0.98
D2053-18-N1-14	0.022674	0.000130	0.001024	0.000016	0.282568	−7.2	−5.4	966	1,490	−0.97
D2053-18-N1-15	0.015955	0.000089	0.000752	0.000015	0.282604	−5.9	−4.2	910	1,411	−0.98
D2053-18-N1-16	0.015500	0.000067	0.000716	0.000014	0.282620	−5.3	−3.6	887	1,374	−0.98
D2053-18-N1-17	0.020414	0.000173	0.000931	0.000016	0.282647	−4.4	−2.7	854	1,315	−0.97
D2053-18-N1-18	0.014041	0.000066	0.000685	0.000014	0.282635	−4.8	−3.1	866	1,342	−0.98
D2053-18-N1-19	0.018124	0.000202	0.000848	0.000017	0.282640	−4.6	−2.9	862	1,331	−0.97
D2053-18-N1-21	0.018563	0.000175	0.000845	0.000015	0.282610	−5.7	−3.9	903	1,396	−0.97
D2053-18-N1-22	0.015701	0.000128	0.000756	0.000015	0.282649	−4.3	−2.6	847	1,310	−0.98
D2053-18-N1-23	0.016880	0.000221	0.000796	0.000017	0.282623	−5.2	−3.5	884	1,367	−0.98
D2053-18-N1-24	0.045235	0.002728	0.001792	0.000018	0.282616	−5.4	−3.8	916	1,384	−0.95
D2053-18-N1-25	0.013856	0.000177	0.000667	0.000015	0.282642	−4.5	−2.8	854	1,324	−0.98
D2053-18-N1-26	0.014896	0.000174	0.000666	0.000015	0.282607	−5.8	−4.1	904	1,404	−0.98
D2053-18-N1-27	0.021796	0.000376	0.000959	0.000016	0.282595	−6.2	−4.5	927	1,430	−0.97
D2053-18-N1-29	0.016932	0.000157	0.000804	0.000016	0.282661	−3.9	−2.1	830	1,282	−0.98
D2053-18-N1-31	0.020664	0.000210	0.000972	0.000013	0.282610	−5.7	−3.9	906	1,396	−0.97
D2053-18-N1-32	0.019233	0.000080	0.000878	0.000017	0.282631	−5.0	−3.2	875	1,351	−0.97
D2053-18-N1-33	0.020872	0.000141	0.000943	0.000015	0.282597	−6.1	−4.4	923	1,425	−0.97
D2053-18-N1-34	0.017832	0.000281	0.000777	0.000014	0.282586	−6.5	−4.8	935	1,450	−0.98
D2053-18-N1-35	0.014667	0.000254	0.000710	0.000015	0.282590	−6.4	−4.7	929	1,442	−0.98

Note: $\varepsilon_{Hf}(t) = 10{,}000 \times \{[(^{176}Hf/^{177}Hf)_S - (^{176}Lu/^{177}Hf)S \times (e^{\lambda t} - 1)]/[(^{176}Hf/^{177}Hf)_{CHUR,0} - (^{176}Lu/^{177}Hf)_{CHUR} \times (e^{\lambda t} - 1)] - 1\}$ $T_{DM} = 1/\lambda \times \ln\{1 + [(^{176}Hf/^{177}Hf)_S - (^{176}Hf/^{177}Hf)_{DM}]/[(^{176}Lu/^{177}Hf)_S - (^{176}Lu/^{177}Hf)_{DM}]\}$ $T_{DM}^{C} = T_{DM} - (T_{DM} - t) \times [(f_{cc} - f_s)/(f_{cc} - f_{DM})]$ $f_{Lu/Hf} = (^{176}Lu/^{177}Hf)_S/(^{176}Lu/^{177}Hf)_{CHUR} - 1$, where $\lambda = 1867 \times 10^{-11}$/a [39]; $(^{176}Lu/^{177}Hf)_S$ and $(^{176}Hf/^{177}Hf)_S$ are the measured values of the samples; $(^{176}Lu/^{177}Hf)_{CHUR} = 00332$ and $(^{176}Hf/^{177}Hf)_{CHUR,0} = 0282772$ [61]; $(^{176}Lu/^{177}Hf)_{DM} = 00384$ and $(^{176}Hf/^{177}Hf)_{DM} = 028325$ [62]; $(^{176}Lu/^{177}Hf)$ mean crust = 0015; $f_{cc} = [(^{176}Lu/^{177}Hf)_{mean\ crust}/(^{176}Lu/^{177}Hf)_{CHUR}] - 1$; $f_s = f_{Lu/Hf}$; $f_{DM} = [(^{176}Lu/^{177}Hf)_{DM}/(^{176}Lu/^{177}Hf)_{CHUR}] - 1$; and t = crystallization time of zircon.

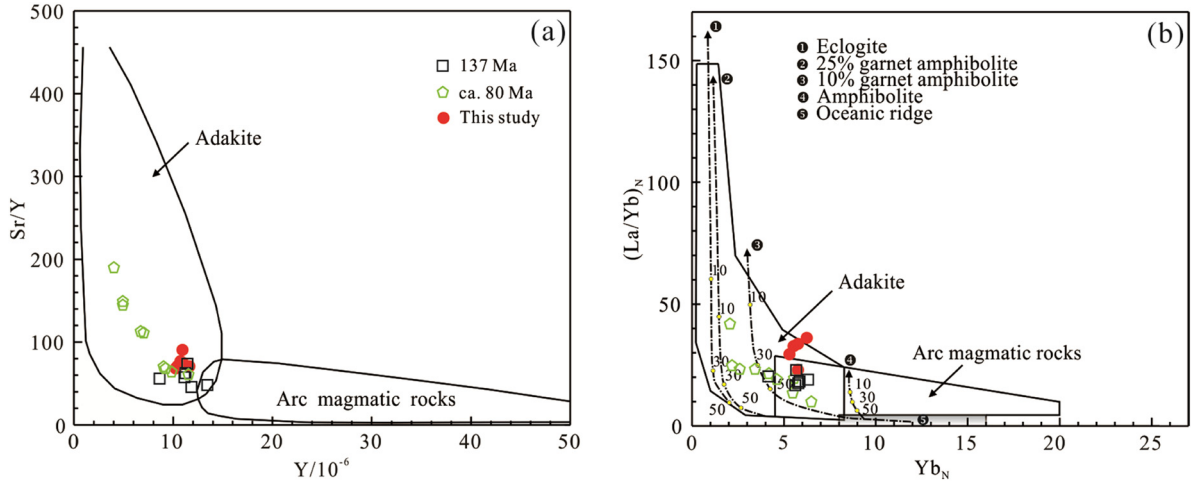

Figure 7: Laimailang monzogranite samples plotted on (a) Sr/Y vs Y diagram [2] and (b) $(La/Yb)_N$ vs Yb_N diagram. Data sources: ca. 80 Ma [14] (lower crust-derived adakitic rocks); 137 Ma [17] (subduction oceanic slab-deriver adakites).

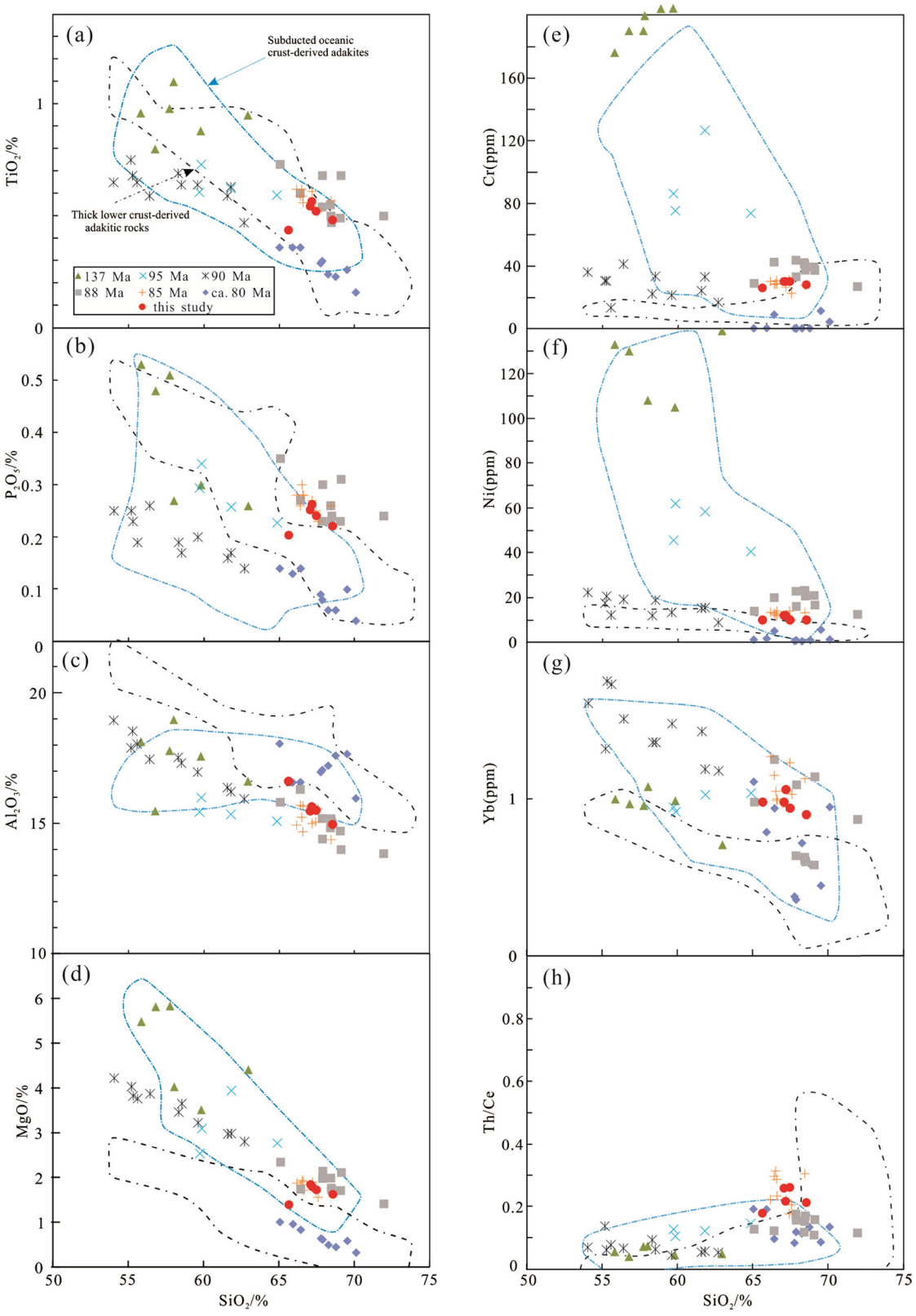

Figure 8: (a–h) Harker variation diagrams showing the major and trace element variations in the Laimailang monzogranite (after Wang et al., 2006). Data sources: typical adakitic rocks on research area: 137 Ma [17]; 95 Ma [16]; 90 Ma [15]; 88 Ma [51]; 85 Ma [19,24]; and ca. 80 Ma [14].

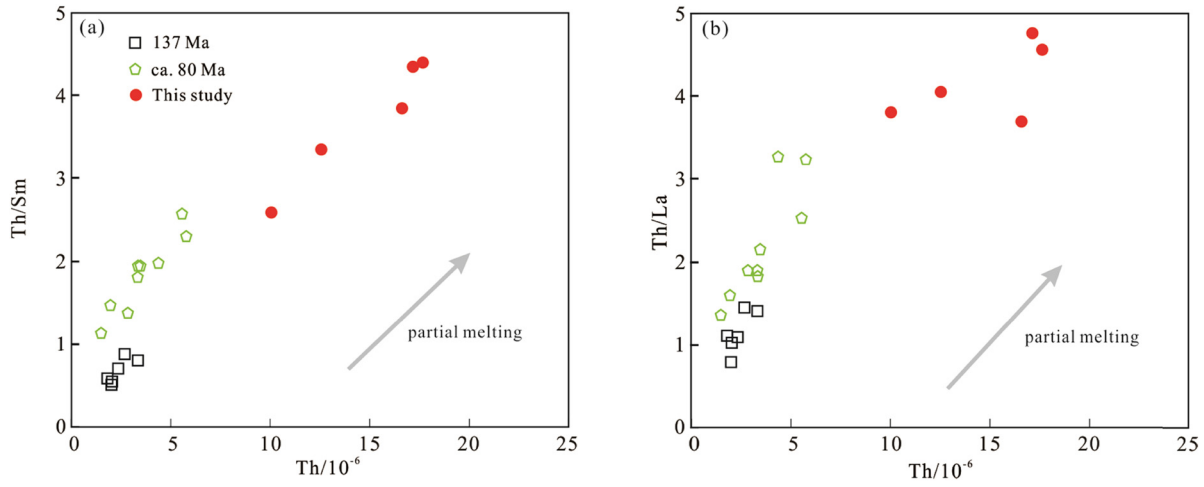

Figure 9: Laimailang monzogranite samples plotted on (a) Th/Sm vs Th diagram and (b) Th/La vs Th diagram. Data sources: 137 Ma [17] (subduction oceanic slab-deriver adakites) and ca. 80 Ma [14] (lower crust-derived adakitic rocks).

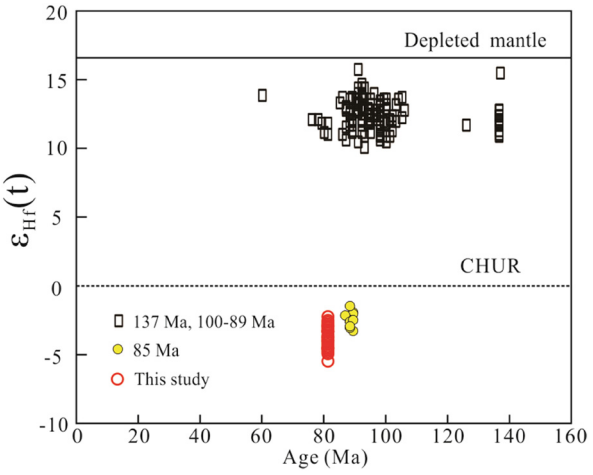

Figure 10: Laimailang monzogranite plotted on zircon $\varepsilon_{Hf}(t)$ vs U–Pb age. Data sources: 137 Ma and 100–89 Ma [17,46] subduction oceanic slab-deriver adakites and 85 Ma [19,24] lower crust-derived adakitic rocks.

garnet remained in the magmatic source [6]. The absence of a pronounced Eu anomaly implies that plagioclase was not a common residual phase [2,41,42]. These arguments suggest that the Laimailang monzogranite formation likely occurred at high-pressure conditions of melting [9,41,43]. Previous studies have shown that this may have been generated from eclogites or garnet amphibolites source region [9]. The ratio of the concentration of a highly incompatible element (e.g., Th) to a moderately incompatible element (e.g., REE, such as La and Sm) can be used to identify partial melting trends [44]. In the (Th/trace-element)-Th diagrams (Figure 9), the Laimailang adakitic rocks define a linear trend, similar to typical Late Cretaceous adakitic rocks in the southern Gangdese, indicating that the magmas were generated by partial melting of the subduction oceanic lithosphere or the lower crust. However, the K_2O contents (most of 2.90–3.77 wt%) of the Laimailang monzogranite differ significantly from the subduction-related adakitic rocks, because adakitic rocks generated by partial melting of the lower crust tend to be K-rich [45] (average 2.78 wt%). Compared to the adakitic rocks in the southern Gangdese derived from partial melting of the subducting oceanic crust, the Laimailang monzogranite is relatively high silica, K rich similar to those of thickened lower crust-derived adakitic rocks (Figure 4).

(2) The zircon $\varepsilon_{Hf}(t)$ value (−2.1 to −5.4) of the Laimailang monzogranite is uniform and negative and old model ages (~1.3–1.4 Ga), which likely originated from partial melting of ancient crustal materials [13]. In fact, the existence of ancient-lower crust in the Lhasa microcontinent further corroborates this suggestion [13]. It is also important to note that the very large negative $\varepsilon_{Hf}(t)$ values (up to −22.0) of zircons in the central Lhasa subterrane [13], which differ significantly from the Laimailang monzogranite. Another piece of evidence is that Mamba (ca. 10 km from Laimailang) mafic enclaves (~85 Ma) are used as the products of mantle-derived magmas, which mixed with crust-derived felsic magmas [24]. In addition, the magmatic activity during the same period of this study has obvious positive isotopic characteristics (Figure 10). All these features indicate that the Laimailang monzogranite is likely to be mainly derived from partial melting of thickened ancient-lower crust, and there is a small amount of enriched fluid-

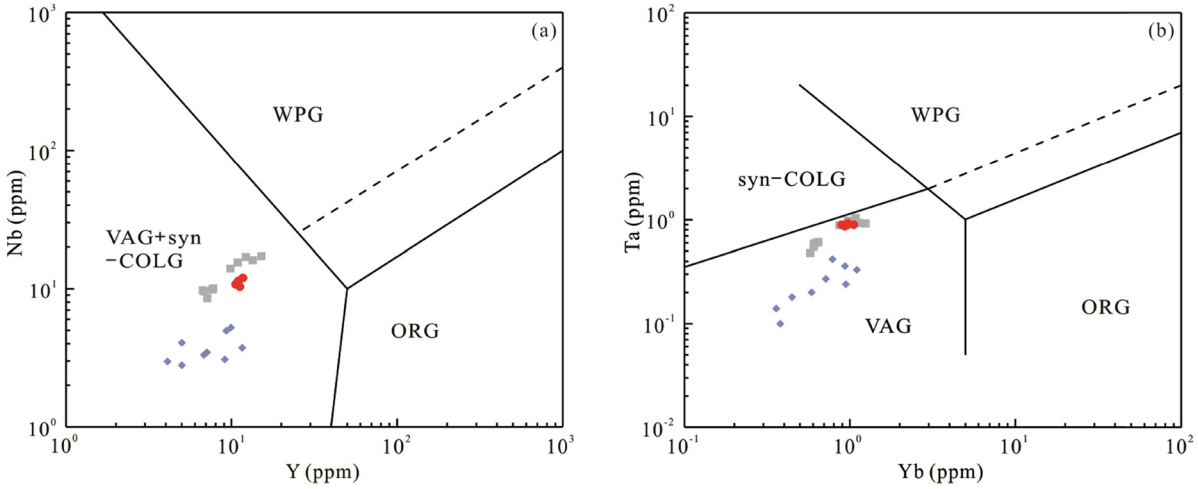

Figure 11: Diagrams of the tectonic setting of trace elements for Laimailang monzogranite (a) Nb vs. Y and (b) Ta vs. Yb (after [46]).

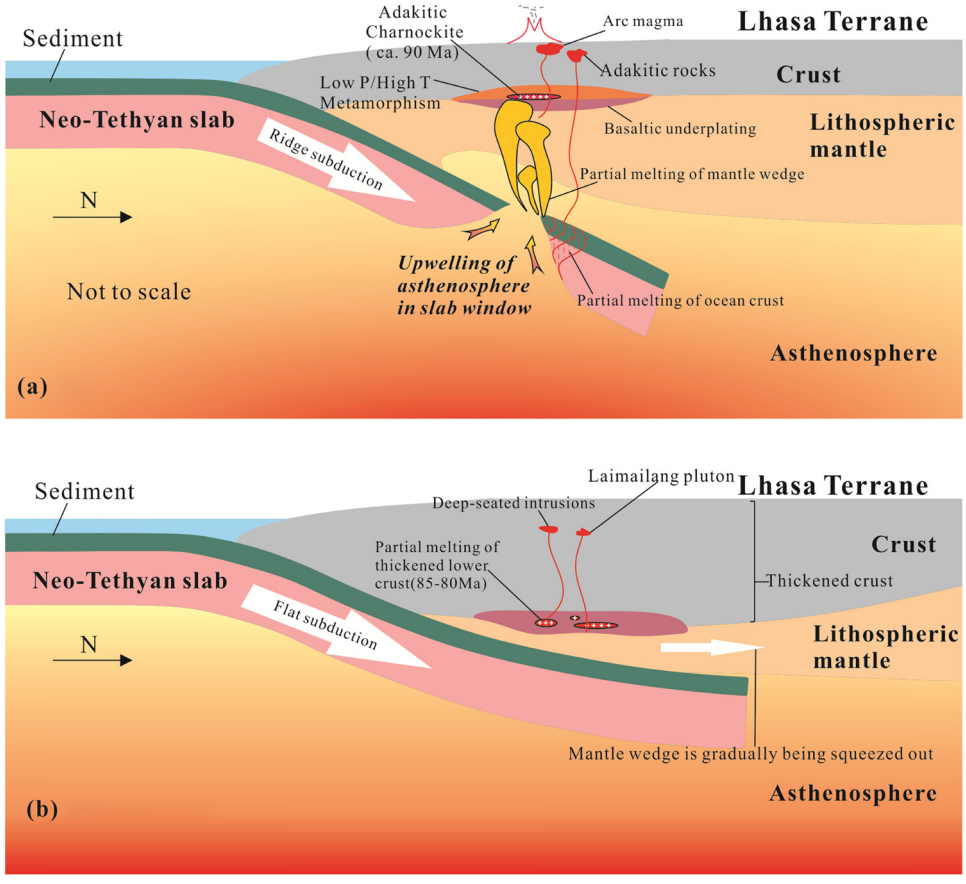

Figure 12: Subduction model for the Neo-Tethyan Ocean in the Late Cretaceous, showing the formation model for the Laimailang adakitic rocks studied here (a) mid-ridge subduction model; (b) thickening of the crust was accompanied by the formation of the Mailang intrusive (adapted from [16,19,29]).

metasomatized mantle magma mixing, resulting in a small negative $\varepsilon_{Hf}(t)$ value.

As the main rocks forming continental crust, granites are closely related to tectonic environment and geodynamic conditions, and some trace elements (such as Rb, Y, Yb, Nb, and Ta) are the most effective elements for the tectonic discrimination of granites due to the sensitivity of these elements to fractional crystallization [46]. The Nb/Y and Ta/Yb diagrams of our samples show the characteristics of

volcanic arc (Figure 11), indicating that the Laimailang monzogranite should be in the subduction background. This is consistent with the previous studies that the Neo-Tethyan Ocean was subducted in the south Gangdese during the Late Cretaceous [11–13].

5.2 Geodynamic interpretation

As mentioned above, zircon U–Pb dating results indicate that a Late Cretaceous (106–80 Ma) magmatic "flare-up" and the subsequent period of magmatic quiescence (80–65 Ma) events occurred in the southern Lhasa subterrane [20,47]. The model of normal (flab or steep angle) subduction can account for much of the Mesozoic magmatism, which generally produces continuous magmatism, but the Late Cretaceous magmatism has obviously magmatic quiescence (80–65 Ma). The existence of 90 Ma extreme high temperature (HT) condition and low H_2O activity charnockites [15,47], which have adakitic affinities, as well as the mafic magmatism (88–85 Ma) [18,24] obtained in southern Lhasa subterrane. That is, the magmatic "flare-up" cannot be explained by normal subduction, which is not coincidence with the extreme high hot. The local region in southern Lhasa terrane lacks the typical ca.85 Ma extension setting rocks, such as A-type granitoids or ocean island basalt, so more evidence is needed for the back-arc extension model [24]. The discovery of mafic rocks and adakites in this area is consistent with the Neo-Tethyan mid-ocean ridge subduction model, given that the rocks indicate HT and require mantle contributions that could be attributed to mantle upwelling through a slab window [48]. Consequently, during which high heat flow as the hot asthenosphere ascends upwards through the slab window and directly heats the subducting oceanic slab and continental crust, leading to partial melting of the oceanic or continental crust along the edges of the slab window [3,49–51]. At the same time, the asthenospheric upwelling induced the appearance of large-scale magmatic rock (e.g., normal calc-alkaline island-arc magmatic rocks and the adakites derived from partial melting of the subducting oceanic slab) in the Late Cretaceous (106–88 Ma) (Figure 12a) [15–18,20–22,52].

However, the Laimailang monzogranite exposure more than 90 km north of the previous trench, which is now represented by the Yarlung-Tsangbo suture zone (IYZSZ, Figure 1). This distance, combined with more than 40% of the major upper crustal shortening in the Cretaceous [53–55], suggests that Laimailang monzogranite was located north of the IYZSZ at a distance of ~200 km or more before Laimailang pluton emplaced (ca. 81 Ma). With such a long distance, the Neo-Tethyan mid-ocean ridge subduction may have had rarely effect on the Laimailang pluton. In the study area, the adakites formed from 85 to 81 Ma thus relate to the partial melting of thickened lower crust ([14,18,19,24]; and this study), which are consistently later than that of the adakites derived from partial melting of the subducting oceanic crust [15–22]. Considering that subduction is a continuous process, these phenomena should be combined to discuss the evolution of the tectonic setting in the local.

Late Cretaceous (106–85 Ma) magmatic "flare-up" can be well explained by an oceanic ridge subduction model, which resulted in the gradual decrease in the plate's subduction angle with HT and positive buoyancy [56], changed to low-angle subduction or flat subduction eventually. This flat-slab stage of the Neo-Tethyan subduction led to a contractional tectonic regime in which the subducting slab may have tectonically thickened the arc crust and squeezed out the mantle wedge; thus, the arc magmatism was terminated [14,57,58]. That is, adakites derived from the thickened lower crust appeared (85–81 Ma) in the south Gangdese ([14,18,19,24] and this study). A magmatic gap or quiescent period occurred between ca. 80 and 68 Ma [14,59], caused by the mantle wedge gradually squeezing out under the flat subduction model. The formation of the Laimailang pluton represents the evolution of the tectonic setting of the Neo-Tethyan oceanic ridge subduction to flat subduction (Figure 12b).

6 Conclusions

Based on zircon U–Pb dating, *in situ* Hf isotopes, and major and trace element geochemistry of the Laimailang monzogranite in the southern Gangdese, as well as previously published data, we can reach the following conclusion:

1. *In situ* zircon U–Pb dating of sample yielded Late Cretaceous ages (ca. 81 Ma) for the Laimailang monzogranite in the southern Gangdese, suggesting a relationship with the subduction of the Neo-Tethyan Ocean.
2. The Laimailang pluton is characterized by high-silica (≥56 wt% SiO_2), K-rich, Na-rich, and high-Al granitoids that are characterized by high Sr, low Y, and HREE contents, and strongly fractionated REE patterns, with no significant Eu anomaly, similar to the adakitic affinities and they may be derived from partial melting of thickened lower crust, interacted with enriched fluid-metasomatized mantle.

3. The formation of the Laimailang pluton represents the evolution of the tectonic setting of the Neo-Tethyan oceanic ridge subduction to flat subduction.

Acknowledgments: We thank the staff of the Zhujiashan studio for their help in the field. This research was funded by the National Science Foundation of China (Grant number 41972118) and the China Geological Survey Project (Grant number DD20160015).

Author contributions: Deliang Li: conceptualization, formal analysis, writing – original draft. Yuanjun Mai: resources, data curation, writing – review and editing. Wenguang Yang: methodology, project administration. Lidong Zhu: supervision, funding acquisition.

Conflict of interest: The authors state no conflict of interest.

References

[1] Kay RW. Aleutian magnesian andesites: Melts from subducted Pacific Ocean crust. J Volcanol Geotherm Res. 1978;4:117–32.
[2] Defant MJ, Drummond MS. Derivation of some modern arc magmas by melting of young subducted lithosphere. Nature. 1990;347(6294):662–5.
[3] Yogodzinski GM, Lees JM, Churikova TG, Dorendorf F, Wöerner G, Volynets ON. Geochemical evidence for the melting of subducting oceanic lithosphere at plate edges. Nature. 2001;409(6819):500–4.
[4] Castillo PR, Janney PE, Solidum RU. Petrology and geochemistry of Camiguin Island, southern Philippines: insights to the source of adakites and other lavas in a complex arc setting. Contrib Mineral Petrol. 1999;134(1):33–51.
[5] Macpherson CG, Dreher ST, Thirlwall MF. Adakites without slab melting: High pressure differentiation of island arc magma, Mindanao, the Philippines. Earth Planet Sci Lett. 2006;243(3–4):581–93.
[6] Rossetti F, Nasrabady M, Theye T, Gerdes A, Monié P, Lucci F. Adakite differentiation and emplacement in a subduction channel: The late Paleocene Sabzevar magmatism (NE Iran). Geol Soc Am Bull. 2014;126(3/4):317–43.
[7] Atherton MP, Petford N. Generation of sodium-rich magmas from newly underplated basaltic crust. Nature. 1993;362(6416):144–6.
[8] Xu JF, Shinjo R, Defant MJ, Wang Q, Rapp RP. Origin of Mesozoic adakitic intrusive rocks in the Ningzhen area of east China: Partial melting of delaminated lower continental crust? Geology. 2002;30(12):1111–4.
[9] Rapp RP, Shimizu N, Norman MD, Applegate GS. Reaction between slab-derived melts and peridotite in the mantle wedge: Experimental constraints at 38 GPa. Chem Geol. 1999;160(4):335–56.
[10] Xiong XL, Adam J, Green TH. Rutile stability and rutile/melt HFSE partitioning during partial melting of hydrous basalt: Implications for TTG genesis. Chem Geol. 2005;218(3–4):339–59.
[11] Chu MF, Chung SL, Song B, Liu DY, O'Reilly SY, Pearson NJ, et al. Zircon U-Pb and Hf isotope constraints on the Mesozoic tectonics and crustal evolution of southern Tibet. Geology. 2006;34(9):745–8.
[12] Ji WQ, Wu FY, Chung SL, Li JX, Liu CZ. Zircon U-Pb geochronology and Hf isotopic constraints on petrogenesis of the Gangdese batholith, southern Tibet. Chem Geol. 2009;262:229–45.
[13] Zhu DC, Zhao ZD, Niu YL, Mo XX, Chung SL, Hou ZQ. The Lhasa Terrane: Record of a microcontinent and its histories of drift and growth. Earth Planet Sci Lett. 2011;301(1–2):241–55.
[14] Wen DR, Chung SL, Song B, Iizuka Y, Yang HJ, Ji JQ, et al. Late Cretaceous gangdese intrusions of adakitic geochemical characteristics, SE Tibet: Petrogenesis and tectonic implications. Lithos. 2008;105(1–2):1–11.
[15] Zhang ZM, Zhao GC, Santosh M, Wang JL, Dong X, Shen K. Late Cretaceous charnockite with adakitic affinities from the Gangdese batholith, southeastern Tibet: Evidence for Neo-Tethyan mid-ocean ridge subduction? Gondwana Res. 2010;17(4):615–31.
[16] Zhang LL, Zhu DC, Wang Q, Zhao ZD, Liu D, Xie JC. Late Cretaceous volcanic rocks in the Sangri area, southern Lhasa Terrane, Tibet: Evidence for oceanic ridge subduction. Lithos. 2019;326–327:144–57.
[17] Zhu DC, Zhao ZD, Pan GT, Lee HY, Kang ZQ, Liao ZL, et al. Early Cretaceous subduction-related adakite-like rocks of the Gangdese Belt, Southern Tibet: Products of slab melting and subsequent melt–peridotite interaction? J Asian Earth Sci. 2009;34(3):298–309.
[18] Guan Q, Zhu DC, Zhao ZD, Zhang LL, Liu M, Li XW, et al. Late Cretaceous adakites in the eastern segment of the Gangdese Belt, southern Tibet: Products of Neo-Tethyan ridge subduction? Acta Petrol Sin. 2010;26(7):2165–79 [in Chinese with English abstract].
[19] Meng FY, Zhao ZD, Zhu DC, Zhang LL, Guan Q, Liu M, et al. Petrogenesis of Late Cretaceous Adakite-like rocks in Mamba from the eastern Gangdese, Tibet. Acta Petrol Sin. 2010;26(7):2180–92 [in Chinese with English abstract].
[20] Zheng YC, Hou ZQ, Gong YL, Liang W, Sun QZ, Zhang S, et al. Petrogenesis of Cretaceous adakite-like intrusions of the Gangdese Plutonic Belt, southern Tibet: Implications for mid-ocean ridge subduction and crustal growth. Lithos. 2014;190–191:240–63.
[21] Dai ZW, Li GM, Ding J, Huang Y, Cao WH. Late Cretaceous adakite in Nuri area, Tibet: Products of rigde subduction. Earth Sci. 2018;43(8):2727–41 [in Chinese with English abstract].
[22] Xu Q, Zeng LS, Gao JH, Zhao LH, Wang YF, Hu ZP. Geochemical characteristics and genesis of the Songka Late Cretaceous adakitic high-Mg diorite in the southern margin of Gangdese, southern Tibet. Acta Petrol Sin. 2019;35(2):455–71 [in Chinese with English abstract].
[23] Jiang ZQ, Wang Q, Wyman DA, Li ZX, Tang GJ, Jia XH, et al. Transition from oceanic to continental lithosphere subduction in southern Tibet: Evidence from the Late Cretaceous Early Oligocene (~91–30 Ma) intrusive rocks in the Chanang Zedong area, southern Gangdese. Lithos. 2014;196–197:213–31.
[24] Meng FY, Zhao ZD, Zhu DC, Mo XX, Guan Q, Huang Y, et al. Late Cretaceous magmatism in Mamba area, central Lhasa subterrane: Products of back-arc extension of Neo-Tethyan Ocean? Gondwana Res. 2014;26(2):505–20.

[25] Yin A, Harrison TM. Geologic evolution of the Himalayan–Tibetan orogen. Annu Rev Earth Planet Sci. 2000;28(1):211–80.
[26] Zhu DC, Zhao ZD, Niu YL, Dilek Y, Mo XX. Lhasa Terrane in southern Tibet came from Australia. Geology. 2011;39(8):727–30.
[27] Wang C, Ding L, Zhang LY, Kapp P, Pullen A, Yue YH. Petrogenesis of Middle–Late Triassic volcanic rocks from the Gangdese belt, southern Lhasa terrane: Implications for early subduction of Neo-Tethyan oceanic lithosphere. Lithos. 2016;262:320–33.
[28] Pan GT, Wang LQ, Zhu DC. Thoughts on some important scientific problems in regional geological survey of the Qinghai-Tibet Plateau. Geol Bull China. 2004;23(1):12–9 [in Chinese with English abstract].
[29] Mo XX, Hou ZQ, Niu YL, Dong GC, Qu XM, Zhao ZD, et al. Mantle contributions to crustal thickening during continental collision: Evidence from Cenozoic igneous rocks in southern Tibet. Lithos. 2007;96(1–2):225–42.
[30] Chappell BW, White AJR. Two contrasting granite types. Pac Geol. 1974;8:173–4.
[31] Pitcher WS. Granite type and tectonic environment. In: Hsü KJ, editor. London: Mountain Building Processes Academic Press; 1982. p. 19–40.
[32] Yuan HL, Gao S, Liu XM, Li HM. Accurate U-Pb age and trace element determinations of zircon by laser ablation-inductively coupled plasma-mass spectrometry. GeostGeoanalytical Res. 2007;28(3):353–70.
[33] Liu YS, Hu ZC, Gao S, Günther D, Xu J, Gao CG, et al. *In situ* analysis of major and trace elements of anhydrous minerals by LA-ICP-MS without applying an internal standard. Chem Geol. 2008;257(1–2):34–43.
[34] Andersen T. Correction of common lead in U–Pb analyses that do not report 204Pb. Chem Geol. 2002;192(1):59–79.
[35] Ludwig KR. User's manual for Isoplot 300: A geochronological toolkit for microsoft excel. Berkeley Geochronol Cent Spec Publ. 2003;4(1):1–70.
[36] Corfu F, Hanchar JM, Hoskin PWO, Kinny P. Atlas of zircon textures. Rev Mineral Geochem. 2003;53(1):469–500.
[37] Hoskin PWO, Black LP. Metamorphic zircon formation by solid-state recrystallization of protolith igneous zircon. J Metamorph Geol. 2000;18(4):423–39.
[38] Morel MLA, Nebel O, Nebel-Jacobsen YJ, Miller JS, Vroon PZ. Hafnium isotope characterization of the GJ-1 zircon reference material by solution and laser-ablation MC-ICPMS. Chem Geol. 2008;255(1–2):231–5.
[39] Söderlund U, Patchett PJ, Vervoort JD, Isachsen CE. The ^{176}Lu decay constant determined by Lu–Hf and U–Pb isotope systematics of Precambrian mafic intrusions. Earth Planet Sci Lett. 2004;219(3–4):311–24.
[40] Le Maitre RW. Igneous rocks: a classification and glossary of terms. 2nd edn. Cambridge, UK: Cambridge University Press; 2002. p. 236.
[41] Martin H, Smithies RH, Rapp R, Moyen JF, Champion D. An overview of adakite, monzogranite–trondhjemite–monzogranite (TTG), and sanukitoid: Relationships and some implications for crustal evolution. Lithos. 2005;79(1–2):1–24.
[42] Castillo PR. Adakite petrogenesis. Lithos. 2012;134–135:304–16.
[43] Sen C, Dunn T. Dehydration melting of a basaltic composition amphibolite at 15 and 20 GPa: implications for the origin of adakites. Contrib Mineral Petrol. 1994;117(4):394–409.
[44] Allégre CJ, Minster JF. Quantitative models of trace element behavior in magmatic processes. Earth Planet Sci Lett. 1978;38:1–25.
[45] Wang Q, Xu JF, Jian P, Bao ZW, Zhao ZH, Li CF, et al. Petrogenesis of adakitic porphyries in an extensional tectonic setting, Dexing, South China: Implications for the genesis of porphyry copper mineralization. J Petrol. 2006;47(1):119–44.
[46] Pearce JA, Harris NBW, Tindle AG. Trace element discrimination diagrams for the tectonic interpretation of granitic rocks. J Petrol. 1984;25(4):956–83.
[47] Ma L, Wang Q, Wyman DA, Li ZX, Jiang ZQ, Yang JH, et al. Late Cretaceous (100–89 Ma) magnesian charnockites with adakitic affinities in the Milin area, eastern Gangdese: Partial melting of subducted oceanic crust and implications for crustal growth in southern Tibet. Lithos. 2013;175–176(8):315–32.
[48] Thorkelson DJ, Breitsprecher K. Partial melting of slab window margins: genesis of adakitic and non-adakitic magmas. Lithos. 2005;79(1–2):25–41.
[49] Delong SE, Schwarz WM, Anderson RN. Thermal effects of ridge subduction. Earth Planet Sci Lett. 1979;44(2):239–246.
[50] Stern CR, Kilian R. Role of the subducted slab, mantle wedge and continental crust in the generation of adakites from the Andean Austral Volcanic Zone. Contrib Mineral Petrol. 1996;123(3):263–81.
[51] Iwamori H. Thermal effects of ridge subduction and its implications for the origin of granitic batholith and paired metamorphic belts. Earth Planet Sci Lett. 2000;181(1–2):131–44.
[52] Liu JH, Xie CM, Li C, Fan JJ, Wang B, Wang W, et al. Origins and tectonic implications of Late Cretaceous adakite and primitive high-Mg andesite in the Songdo area, southern Lhasa subterrane, Tibet. Gondwana Res. 2019;79(C):185–203.
[53] Ratschbacher L, Frisch W, Chen CS. Deformation and motion along the southern margin of the Lhasa block (Tibet) prior to and during the India-Asia collision. J Geodyn. 1992;6(1–2):21–54.
[54] Murphy MA, An Y, Harrison TM, Dürr SB, Chen Z, Ryerson FJ, et al. Did the Indo-Asian collision alone create the Tibetan plateau? Geology. 1997;25(8):719–22.
[55] Kapp P, Decelles PG, Gehrels GE, Heizler M, Ding L. Geological records of the Lhasa-Qiangtang and Indo-Asian collisions in the Nima area of central Tibet. Geol Soc Am Bull. 2007;119(7–8):917–33.
[56] Bourdon E, Eissen JP, Gutscher MA, Monzier M, Hall ML, Cotton J. Magmatic response to early aseismic ridge subduction: The Ecuadorian margin case (South America). Earth Planet Sci Lett. 2003;205(3–4):123–38.
[57] Booker JR, Favetto A, Pomposlello MC. Low electrical resistivity associated with plunging of the Nazca flat slab beneath Argentina. Nature. 2004;429:399–403.
[58] Kay SM, Mpodozis C. Central Andean ore deposits linked to evolving shallow subduction systems and thickening crust. GSA Today. 2001;11(3):4–9.
[59] He SD, Kapp P, Decelles PG, Gehrels GE, Heizler M. Cretaceous–Tertiary geology of the Gangdese Arc in the

Linzhou area, southern Tibet. Tectonophysics. 2007;433(1):15–37.
[60] Sun SS, Mcdonough WF. Chemical and isotopic systematics of oceanic basalts: implications for mantle composition and processes. Geol Soc London Spec Publ. 1989;42(1):313–45.
[61] Blichert-Toft J, Albarède F. The Lu-Hf geochemistry of chondrites and the evolution of the mantle-crust system. Earth Planet Sci Lett. 1997;148:243–58.
[62] Griffin WL, Pearson NJ, Belousova E. The Hf isotope composition of cratonic mantle: LAM-MCICPMS analysis of zircon megacrysts in kimberlites. Geochim Cosmochim Acta. 2000;64:133–47.